Fabrication and Performance of Silicon Immersion Gratings for Infrared Spectroscopy

Jasmina P. Marsh, Douglas J. Mar, Daniel T. Jaffe
Department of Astronomy, Univ. of Texas at Austin, 1 University Station C1400, Austin, TX 78712

ABSTRACT

Silicon immersion gratings open up the possibility of compact infrared spectrometers with high throughput, high spectral resolution, and extensive instantaneous coverage. The performance of the diffraction gratings that we have been developing over the past 15 years has reached the level where it can exceed that of commercially available diffraction gratings. We have produced science-grade immersion grating echelles with coarsely spaced grooves on silicon substrates appropriate for applications in the near-infrared (1.1-5 μm). Devices in the current generation have excellent throughput (60%-80%) and display diffraction-limited performance over apertures of 20 mm or more. Tests of the gratings done in reflection are in good agreement with tests done in immersion. We assess the current state of the silicon grating technology as well as discuss further developments necessary for making gratings on larger silicon substrates.

Keywords: immersion grating, silicon, infrared spectroscopy, high resolution

1. INTRODUCTION

Current high resolution spectrographs for observations in the near infrared (IR) at λ = 1-5 μm include PHOENIX[1] on Gemini South, CSHELL[2] on NASA's Infrared Telescope Facility (IRTF), NIRSPEC[3] on Keck 2, and CRIRES[4] on the VLT. Of these, NIRSPEC is a cross-dispersed spectrograph while the other three are single order instruments. None offer continuous spectral coverage of more than a small fraction of the wavelength range within a given atmospheric window. The maximum resolving powers of these instruments ranges from 30,000 to 70,000. To realize gains in resolving power without narrowing the slit, new spectrographs require larger grating lengths.

There is a need in the astronomical community for a cross-dispersed near-IR instrument with high resolving power (up to 100,000) and with simultaneous coverage of a large range of continuous wavelengths. Immersion gratings can fill this need. These devices are reflection gratings in which light passes through a medium with refractive index *n* before hitting the diffraction grating. They offer two distinct advantages over conventional gratings: (1) they have higher diffraction limited resolution (by a factor of the refractive index *n*) than a comparable conventional front surface grating and therefore permit compact spectrograph designs with high resolving power and, (2) because they can have very coarse grooves, they enable continuous wavelength coverage in cross-dispersed modes. Silicon is an especially attractive material from which to fabricate immersion gratings, because of its large refractive index n = 3.4 and its transparency in the near-IR[5,6]. Silicon immersion gratings are an enabling technology for the next generation of high resolution IR spectrographs such as ImGES (proposed for the NASA-IRTF) and HRNIRS (proposed for Gemini). In this work, we report on the status of our efforts to fabricate immersion gratings suitable for high-resolution near-IR instruments and on the performance of two resulting devices.

JPM: jasna@astro.as.utexas.edu
DJM: djmar@astro.as.utexas.edu
DTJ: dtj@astro.as.utexas.edu

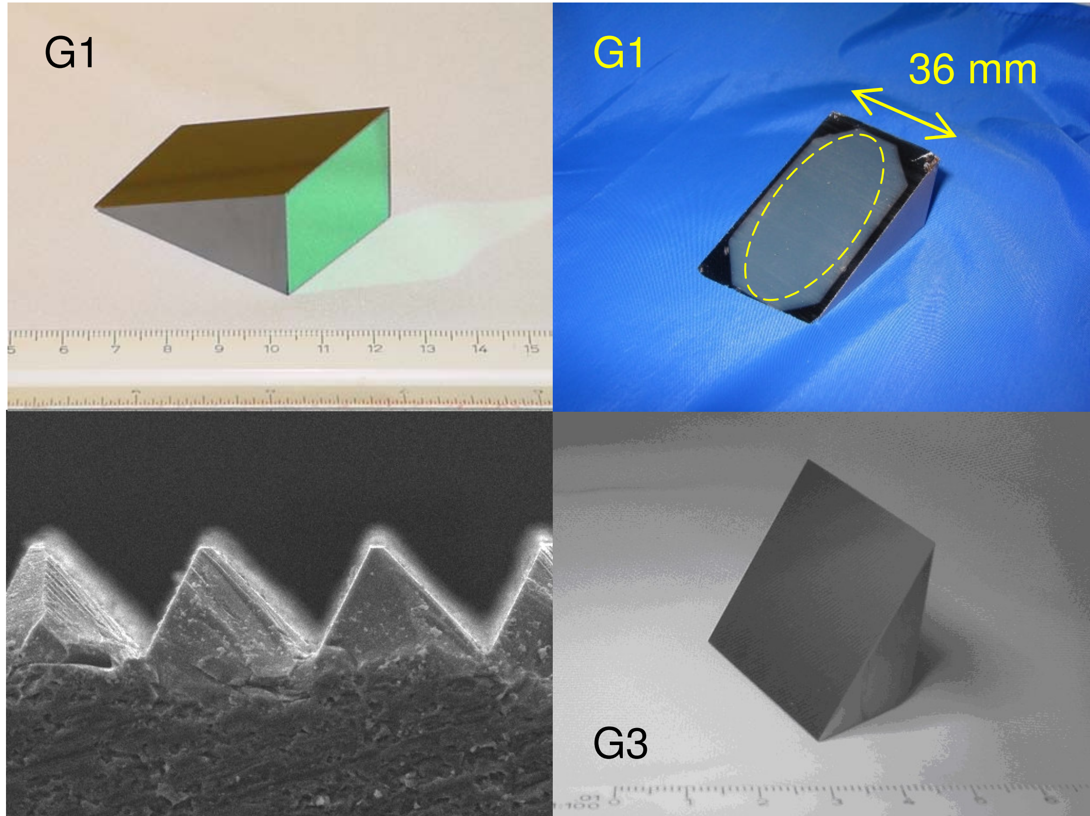

Figure 1. Images of silicon immersion grating devices. The upper left image shows G1 shaped to its finished R2 prism, with grating angle δ = 63.4º between the entrance face and the grating surface. The entrance face is polished and coated with a broadband anti-reflection coating optimized for 1.2-5 µm. The grating surface of G1 has not yet been metallized and appears dark in the image. The upper right image shows G1 after an aluminum reflection coating was deposited on the grating surface. The ellipse illustrates the projection of a 23 mm aperture onto the grating surface. In the lower left, a scanning electron microscope (SEM) micrograph shows the detail of the grooves etched into a silicon wafer witness. This witness grating is blazed at δ = 63.4º and has groove spacing σ = 80 µm, the same parameters as for G1. The lower right image shows G3, a silicon grating with δ = 32.6º and σ = 87 µm. Its entrance and grating faces are uncoated, and it can be tested either as a grism in transmission[7] or as an immersion grating. The 37 mm × 32 mm ruled area of G3 can accommodate a 25 mm diameter beam.

2. FABRICATION

In this paper, we focus on two silicon grating devices called G1 and G3, shown in Fig. 1. The fabrication process involves many steps, some of which are detailed elsewhere[7-12]. Here we provide details relevant for the fabrication of immersion gratings. We start from a 76 mm diameter cylindrical ingot of monocrystalline float-zone silicon with resistivity 2000 ohm-cm. The ⟨111⟩ crystal growth axis of the ingot coincides with the cylinder axis to an accuracy of ~1°. We therefore use x-ray diffractometry was used to determine the orientation of the ingot to within 0.03-0.04° and grind a long (40-50 mm) precision flat running the length of the ingot on the Si (110) surface. In subsequent lithography steps, this flat serves as a precise alignment marker. The ingot is then mounted on this precision flat, rotated to the desired blaze, and sliced into elliptical blanks of thickness sufficient to entirely contain the final prisms. The exposed surfaces are ground, etched, and polished flat to surface figures approaching 1/100 waves rms at λ = 632.8 nm. The polishing is done by chemical-mechanical planarization (CMP), which results in less sub-surface damage to the crystal lattice. The blanks are then coated with a ~60 nm ± 5% layer of low pressure chemical vapor deposition (LPCVD) silicon nitride as a passivation layer.

2.1. Grating fabrication

Once the blanks are prepared, we pattern of a series of periodic lines in the silicon nitride. This is accomplished by contact photolithography. For each grating, the blank is cleaned, baked to dehydrate the surface, and spin-coated with hexamethyldisilazane (HMDS) primer. A novolak resin photoresist is then spin-coated onto the blank. A flat quartz mask with a pattern of parallel chrome lines on it is carefully placed in contact with the blank. The lines are aligned perpendicular to within 0.1° to the Si (110) flat by viewing the lines and the edge of the flat through a stereomicroscope. This angular precision prevents dislocations from appearing during the wet-etch micromachining process that creates the grooves. Achieving good contact across the entire pattern between the photoresist layer and the mask is challenging. The photoresist is exposed to ultraviolet light through the quartz mask. The exposed areas of the photoresist are removed by immersing the blank in a tetramethyl ammonium hydroxide (TMAH) developer, thereby transferring the desired grating pattern to the photoresist layer. This layer is then used as a mask in a dry plasma etcher, where unprotected areas of the silicon nitride layer are removed. This etch step transfers the line pattern to the silicon nitride. Although these photolithographic steps are similar to industrial processes developed for semiconductor VLSI electronics and micro-electro-mechanical systems applications, those processes are designed for thin wafers, and must be adapted to accommodate the unusual shape and bulk of our blanks, which are elliptical, slanted, and have masses up to several hundred grams. Our custom built spin table must be able to accelerate blanks that have moments of inertia that are one to two orders of magnitude larger than those of typical wafer substrates. The slanted elliptical shape of the blanks can be difficult to mount and balance on the spin table, and aerodynamic effects at the elliptical edge can degrade the uniformity of the spun photoresist layer. We constructed custom holders for each blank thickness and used a fairing to reduce the aerodynamic problems. The UV mask aligner is also custom built to handle substrates with thickness up to 35 mm. In the plasma etcher, we used focusing rings to improve the etch uniformity and etch rate.

The patterned silicon nitride layer serves as an etch mask through which an anisotropic wet etch based on potassium hydroxide and isopropanol can chemically micromachine grooves into the silicon surface. The custom apparatus used for this step combines an ultrasonic agitator with a heated re-circulating water bath that maintains the temperature of the etch container and the silicon blank at 68°C, a temperature chosen to maximize the etch anisotropy. The ultrasonic agitation and the isopropanol both promote the detachment of hydrogen gas bubbles that are formed during the etching process, helping to optimize the flatness and smoothness of the grooves. From SEM images of the etch undercut, and measurements of the groove vertex angle using a stylus profilometer, we determined that the etch anisotropy R_{100}/R_{111} = 69, where the R's are the etch rates in the two crystal directions. The finite etch anisotropy leads to a shift in the groove alignment and consequently, a shift in the blaze angle. For example, at λ = 2 µm for an R2 silicon immersion grating operated in 247th order, the blaze wavelength shifts from 1.998 µm for δ = 63.4° to 1.991 µm for δ = 63.0°, a shift of -0.007 µm, or approximately one full order. This effect must be taken into account in the design and in the ingot orientation in order to achieve the desired final blaze angle.

2.2. Device fabrication

After washing the etched grating in hot (150°C) concentrated phosphoric acid to remove any remaining silicon nitride and other leftover debris from the wet etch, the grating is fully formed and the disk is ready to be shaped into a prism. The entrance face is oriented nearly parallel but not exactly to the grating facets, as a small γ tilt is desirable to separate the direction of the output beam at the blaze wavelength from the residual reflection off the entrance face. The entrance face is polished to optical flatness (surface figures less than 1/20 waves rms at 632.8 nm). The bottom face of the prism is formed with a small tip angle and a cosmetic polish to control the directions of any stray light diffracted from the grating surface.

To finish the immersion gratings, coatings are necessary to optimize the infrared throughput. A broadband anti-reflection (BBAR) coating on the entrance reduces the index mismatch losses between the silicon and the surrounding vacuum. As shown in the upper left panel of Fig. 1, we apply a commercial 1.0-5.0 µm BBAR coating to the entrance face of G1. This coating is designed to have 2% average reflection from 1.2 to 4.9 µm. The measured reflectance of the coating meets this design goal and averages about ~2% from 1.0 to 5.0 µm with a maximum of 3.0% at 1.2 µm. We then apply a reflective aluminum coating to the groove surfaces (see Fig. 1, upper right). Using SEM micrographs of sputtered Al films on Si witnesses (see Fig. 2), we have verified that these sputtered aluminum layers cover the grating completely, are free from voids, and despite their granular exterior, have smooth underside surfaces against the Si

groove facet. We have also assessed the durability and cryogenic performance of the BBAR and Al coatings by subjected coated Si witnesses to multiple rapid thermal cyclings to 77 K by dunking into liquid nitrogen in air, without significant damage (see right panel of Fig. 2).

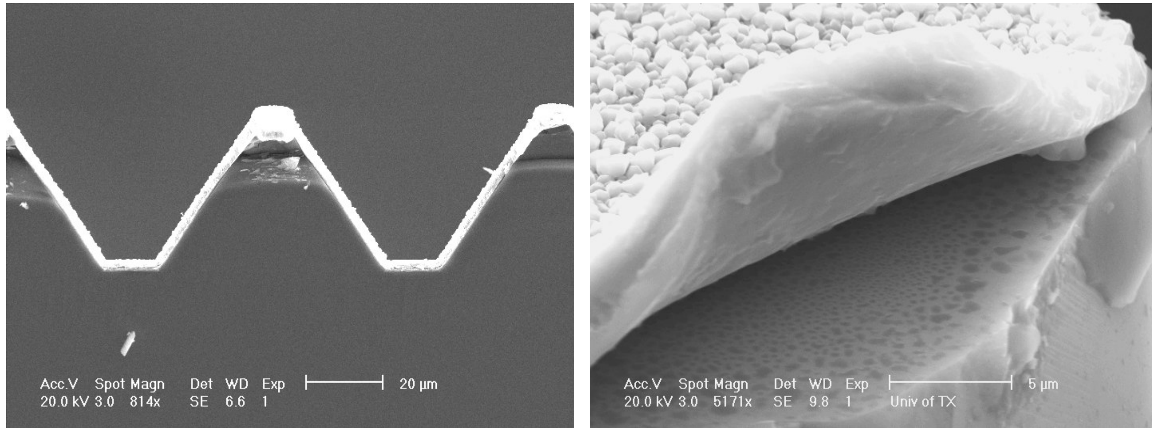

Figure 2. SEM micrographs of an aluminized grating on a Si witness grating, showing several grooves (left) and a corner detail of one groove (right). In the left figure, the silicon is at the bottom of the figure and has been incompletely etched. The bright Al layer is contiguous and completely covers the grating facets, and has a thickness of approximately 2 µm. In the right figure, the top layer of the Al coating is granular, while the underside is smooth. Near the edge of the wafer, the Al layer has only just begun to delaminate after dozens of successive rapid thermal cycles between room temperature and 77 K. The rest of the Al layer (not shown) remained intact. Of course, a real grating would not be ordinarily subjected to such brutal thermal treatment.

3. OPTICAL EVALUATION

Our laboratory test setup consists of two bench spectrographs, each with a layout identical to that of a Twyman-Green interferometer. The first spectrograph uses a green HeNe laser (543.5 nm) and the second uses an IR HeNe laser (1523 nm) as a light source. In both setups, light from the lasers is collimated and passes through an iris of diameter D to accommodate different apertures of the test optics. For the visible laser, D = 25 mm. For the IR setup, the beam size is 10 mm, limited by the IR collimator. Beam splitters in both setups direct light into two arms, one of which contains a reference mirror and the other contains the grating under test. Light from both spectrograph arms is simultaneously focused either onto a visible CCD array (1024×1024 format, 13 µm pixels) or an InGaAs array camera (320×256 format, 30 µm pixels, 0.9-1.7 µm) and recorded as a monochromatic spectrum.

3.1. Immersion efficiency

For the immersion gratings, we measure the throughput efficiency when used in immersion. This quantity is the relative amount of infrared light that is diffracted from the grating and re-emerges from the prism, compared to the intensity incident on the device. Collimated laser light enters the entrance face of the immersion grating, is diffracted from the grating, and re-emerges from the device. Because our laser wavelength λ = 1523 nm is not on the blaze for these gratings, each spectrum consists of a series of orders. The diffracted beams are focused by a f = 125 mm lens to form a 2D image on the infrared camera array. Usually, 2-10 orders are recorded. These images are collapsed in the cross-spectral direction to form 1-dimensional spectra, as shown in Fig. 3.

For each device, we obtain an estimate of the device throughput by summing up the power in the series of diffracted orders and comparing the total to the power measured in the incident beam. The result is approximately equal to the return signal that one would observe in a single order for a laser at the blaze wavelength. The camera field-of-view restricts us to using only the brightest orders, so that the measurement is actually a lower limit on the blaze efficiency. Table 1 contains the relative immersion throughput η of each grating at λ = 1.523 µm, compared against the measured light in the 10 mm beam. The raw throughput is simply the light out divided by the light in for the devices in their

current state (G1 equipped with BBAR and metallized, and G3 uncoated). The final column is an estimate of the throughput after correction for power in orders not directly measured (2-6%), and in the case of G3, by further assuming that it is equipped with a BBAR coating with 2% loss and a metallic layer on the grating facets. It is clear that both gratings have excellent throughput, and we expect that G3 will achieve better than 80% throughput in immersion at λ = 2 µm.

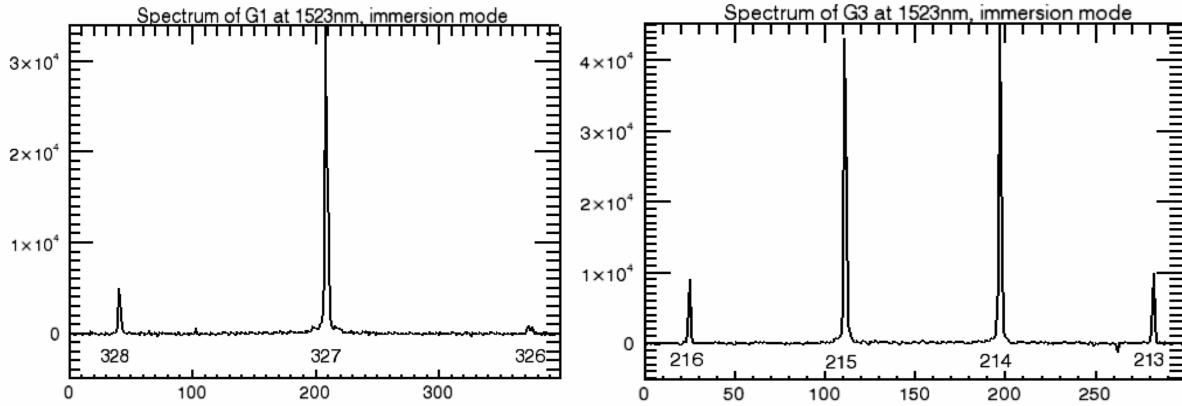

Figure 3. Monochromatic immersion spectra of G1 and G3, obtained using a collimated beam of 10 mm light with λ = 1.523 µm. The x-axis gives position along the spectrum in pixels. Order numbers are indicated at the base of each peak. The y-axis gives intensities integrated over several rows in the cross-dispersion direction.

Table 1. Measured efficiencies at λ = 1.523 µm for gratings G1 and G3, obtained from the immersion spectra in Figure 3. The raw measurement indicates the measured output power divided by the input intensity for the devices in their current state (G1 complete, G3 uncoated). These raw efficiencies give the throughput at the blaze wavelength. The estimated efficiencies adjust the raw efficiencies by including an estimate of the power in orders not directly measured, and in the case of G3, a correction for reflection losses incurred by the light due to index mismatch as the beam enters and exits the device. This estimate for G3 assumes that these losses are reduced by applying the same BBAR (2% loss) and metallic layers to G3.

device and current state	η_{raw}	η_{est}
G1, with 1-5 µm BBAR @ 2% loss and metallized	68%	71%
G3, uncoated	39%	82%

3.2. Resolving power and point spread function

Visible wavelength interference analysis of the grating was done with a commercial optical interferometer. This was a very valuable tool for evaluating the wavefront quality of our gratings and predicting the point spread function (PSF). The light source for the interferometer is a HeNe laser at λ = 632.8 nm and therefore limited to reflection measurements of the gratings. This reflection data, however, can be used to evaluate the grating quality over large areas and can be used to predict the PSF performance in immersion at various wavelengths. In Figure 4 we show surface error plots for G1 and G3. The rms surface figures are extremely good (λ/39 and λ/100 at λ = 632.8 nm) over the full 25 mm aperture. These surface variations should be compared to the internal wavelength in the immersion grating, i.e. an internal wavelength of 632.8 nm corresponds to an application wavelength of ~2.1 µm.

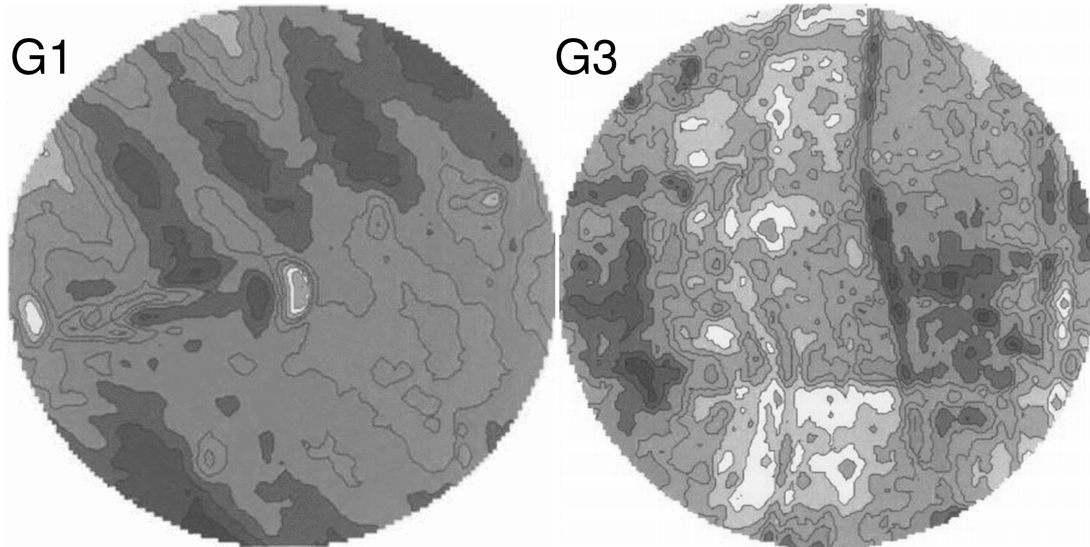

Figure 4. Surface error plots of G1 and G3 taken with an interferometer using laser light at $\lambda = 632.8$ nm. Each circle is a 25 mm aperture. Contours correspond to $\lambda/45$ and $\lambda/157$ for G1 and G3 respectively. The rms surface figures over these areas are $\lambda/39$ and $\lambda/100$, respectively.

The surface error measurements can be transformed and scaled to obtain the predicted PSF for performance in immersion at a particular wavelength. Figure 5 shows the PSF of G1 predicted from the error map in Fig. 4 in the right panel, and the PSF of G1 directly measured in immersion at $\lambda = 1523$ nm. This measurement is performed with the same setup as for the data in Fig. 3, but using a slower camera lens ($f = 838$ mm) to produce a diffraction limited image of the brightest order on the IR array. The interferometer gives a fairly accurate picture of what the grating performance is in immersion and is a powerful tool to assess the surface figure of the gratings before they are cut and shaped into prisms. Surface plots of the entire area of the etched grating help us to extract the best portion of the grating for the device and can also help diagnose any problems in fabrication procedures.

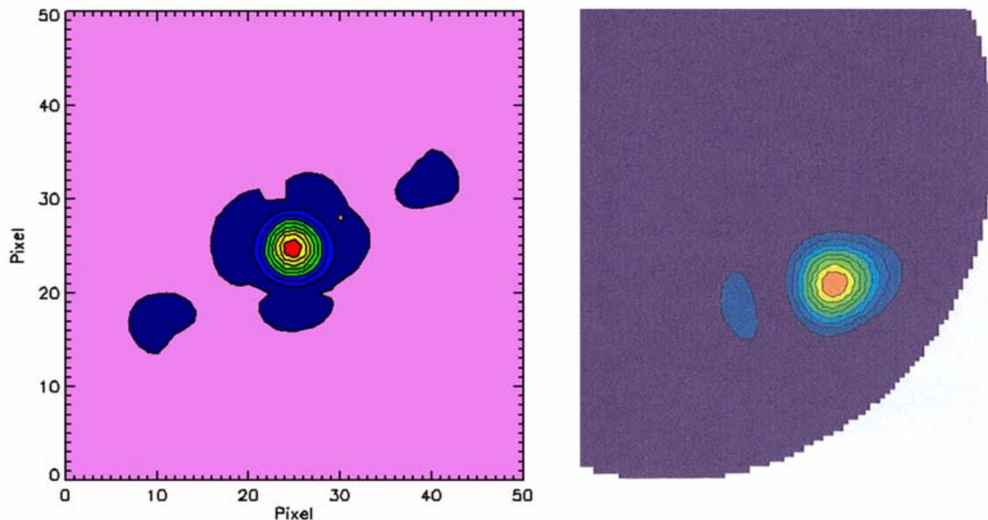

Figure 5. Comparison of PSF for G1 as measured directly at $\lambda = 1.523$ μm (left) and the PSF inferred by transforming the surface error map obtained from optical interferometer measurements.

The diameter of the Airy disk is $1.22\lambda f/(D\Delta x) = 5.2$ pixels where D is the beam diameter and $\Delta x = 30$ μm is the pixel size for the IR camera. Images such as the one measured for the PSF of G1 (left panel of Fig. 4) were dark subtracted, and the profile of the diffraction spot was fit by a 2-dimensional Gaussian function in order to measure its width. The results of this step are summarized in Table 2. The predicted resolving power is computed as $R_p = 2nD\tan\delta/\lambda$ and the demonstrated resolving power, R_d, was calculated using the formula $d\beta/d\lambda = 2n\tan\delta/\lambda$ for angular dispersion in the Littrow mode and correcting for pixel sampling. We obtain $R_d = \lambda/\Delta\lambda = 2n\tan\delta/x$, where x is the product of Δx and the FWHM of the spot measured in pixels. As shown, demonstrated measured resolving powers of as much as 75,000 at 1.523 μm have been obtained.

Table 2. Measurements of the immersion PSF at $\lambda = 1.523$ μm, demonstrated and predicted resolving power, and Strehl ratios obtained for the immersion grating devices G1 and G3. The first row lists comparison measurements for a Si mirror.

device	FWHMx	FWHMy	R_d	R_p	Strehl ratio	
					IR PSF	interferometer
mirror	4.78	4.90				
G1	5.10	4.79	75,400	90,500	0.91	0.90
G3	4.74	4.90	26,000	28,900	0.99	1.00

The next step is to obtain 1-dimensional PSFs (Fig. 6) by summing over 10 pixels in the cross dispersion direction around the peak of the diffraction spot in order to determine the Strehl ratios of G1 and G3. The Strehl ratio is defined as the peak value of intensity (normalized to the total power in the PSF) for an aberrated image relative to its value for an unaberrated image. Optical systems with a Strehl ratio greater than 0.8 are usually considered diffraction limited. A system with a Strehl exceeding 0.8 would have an RMS wave front error of less than $\lambda/14$. We calculated the area under the 1D spectral PSF for each grating and normalized the PSF by the ratio of that area to the area under the (unaberrated) mirror PSF. The peak value of the normalized grating PSF is the Strehl ratio. The Strehl ratios for gratings G1, and G3 are listed in Table 2. The last two columns contain values of Strehl ratios measured directly from the infrared spectra at $\lambda = 1.523$ μm in immersion (Fig. 5) and determined from the interferometric wavefront error measurements (Fig. 4) at $\lambda = 632.8$ nm. They are in excellent agreement.

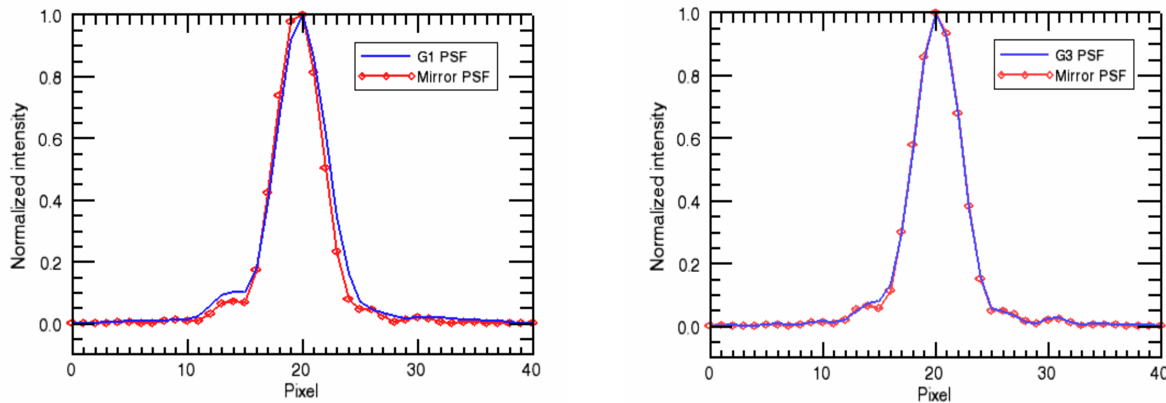

Figure 6. Monochromatic 1-dimensional point spread functions (PSF) of G1 and G3, taken in immersion at $\lambda = 1.523$ μm using a collimated beam of 10 mm. Data for the silicon gratings are shown as a solid line, while the data for a reference mirror is shown with symbols. The x-axis gives position along the spectrum in pixels. The y-axis gives intensities integrated over ten pixel rows in the cross-dispersion direction. The close agreement between the grating PSFs and those for the mirror indicate diffraction-limited performance over a 10 mm diameter.

We conclude that the performance of G1 and G3 is diffraction limited at 1.523 μm when the devices are used as immersion gratings. The agreement between the front surface tests using the optical interferometer and the direct immersion tests is another confirmation of our method that uses front surface measurements, both spectroscopic and interferometric, to test and predict the performance of echelles in immersion.

3.3. Grating aberrations and defects

Errors in the groove shape and spacing and groove surface roughness are factors that degrade the performance of diffraction gratings by lowering their efficiency and causing unwanted features in the observed spectra. These errors and defects manifest themselves as grass, ghosts, satellites, and diffuse scatter[13]. We discuss our observations of these errors as well as ways to improve the performance of future gratings.

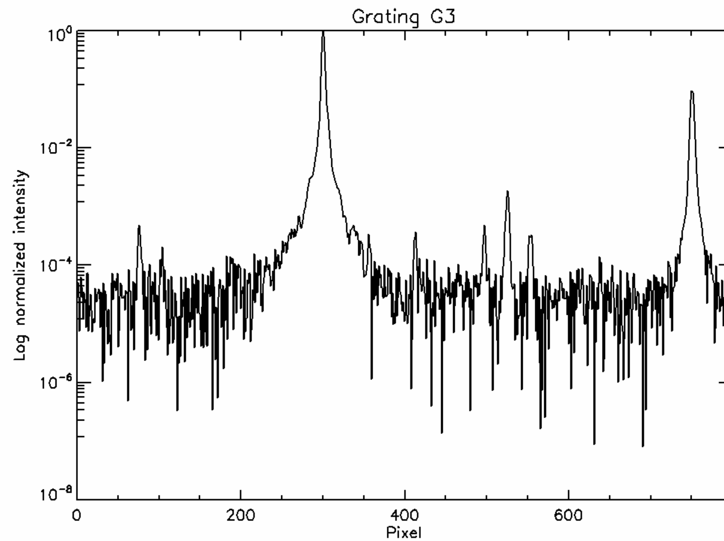

Figure 7. High signal-to noise monochromatic spectrum of G3 taken in reflection at λ = 543.5 nm. Thousands of exposures were summed to beat down the background noise. The vertical axis is logarithmic, and the data have been normalized to unity at the brightest order. No features are visible between the orders down to a level of 2×10^{-4}.

3.3.1. Grass

Random errors in groove positions cause grooves to be slightly displaced from their ideal positions. These displacements introduce phase errors that transfer power from the diffraction peak into the entire blaze which, in a monochromatic spectrum, makes it appear as light between diffraction spikes representing the individual orders (Fig. 7). We have previously observed this "grass" in the spectra of prototype gratings and found, as expected, that the intensity distribution of light in the grass matches that of the blaze function for a single groove[11]. In this paper, we estimated the fraction of light in the grass, η_{grass}, from our spectra by integrating over 10-20 rows of the spectrum images to obtain a 1D spectrum (the same method we used to measure efficiencies), and then subtracting out previously determined efficiencies in observed orders as well as any observed ghosts. The angular range of integration in the cross dispersion direction was only 0.07° so any diffuse scattered light, while it may raise the value of light intensity scattered in the grass, should not contribute to it significantly. Measured values for scattered light in grass are given in Table 3. The intensity of light in the grass is given by[13]:

$$\frac{\eta_{grass}}{\eta_0} = \left(\frac{2\pi}{\lambda} 2\varepsilon_{spacing} \sin\delta \right)^2$$

assuming a Gaussian distribution of spacing errors where $\varepsilon_{spacing}$ is the rms groove position error. Using the above equation, we estimated $\varepsilon_{spacing}$, using the measured values of η_{grass}. The theoretical blaze efficiency η_0 is the return expected for a perfect grating of a given groove geometry. The groove geometry of G1 and G3 and the wavelength of 543.5 nm in reflection result in η_0 of 88% and 91% respectively. The groove spacing error, $\varepsilon_{spacing}$, represents the accuracy with which we can position lines in the passivation layer and subsequently etch grooves. We immediately notice that the random spacing errors, $\varepsilon_{spacing}$, derived from the observed grass intensity are both very small and close to the same value for all three gratings. This result implies that we have good control over the pattern transfer process and good repeatability, even for thick silicon substrates. The total measured errors, ε_{phase}, derived from the optical interferograms, are larger than the spacing errors and differ more strongly between the gratings. As we will show, the larger values of ε_{phase} derived for G1 result from repetitive errors which produce ghosts rather than grass (see Section 3.3.3).

Table 3. Scattered light due to random errors in groove positions.

device	grass level	$\varepsilon_{spacing}$	ε_{phase}	ε_{phase} from interferograms
G1	4.6%	12 nm	11 nm	33.0 nm
G3	1.9%	13 nm	6.9 nm	6.3 nm

3.3.2. Diffuse scattered light

Any deviation in the height of a groove from a perfectly smooth surface up to scale sizes of the order of λ is called groove microroughness. Small scale roughness of the groove surfaces causes incident light to be scattered in random directions. In extreme cases where the amount of scattered light is large, we can observe a halo around the center of the spectrum. More typically, the large angular scale of the diffuse scattered light makes it very difficult to perform direct measurements. Instead, we use physical measurements such as surface profilometry and atomic force microscopy (AFM) to measure the surface roughness ($\varepsilon_{roughness}$) of the grooves. We have done this for G2[7], a silicon grism blazed at 6.16º, but due to constraints on the sample height in the test equipment, we are unable to measure G1 and G3. We measured average $\varepsilon_{roughness}$ of 1.7 nm on a 2 μm × 2 μm area of groove surface for G2. The total integrated scattering is given[14] approximately by:

$$\frac{I_{diffuse}}{I_0} = \left(\frac{2\pi n}{\lambda} 2\varepsilon_{roughness} \right)^2$$

where $\varepsilon_{roughness}$ is the RMS surface roughness as measured by the AFM. The predicted total integrated scattered light, $I_{diffuse}$, for G2 is estimated to be 0.1% at 632.8 nm and 0.04% at 3.5 μm using Eq. 4. These are lower limits but likely close to the values for diffuse light due to microroughness for G1 and G3.

3.3.3 Ghosts

When grooves are displaced from the perfect spacing σ with a periodic variation, they result in the appearance of secondary images or ghosts. When ghosts are near the parent line, they are called Rowland ghosts. Ghosts observed in spectra in our early gratings[8,11] were attributed to periodic errors in the mask. We consequently acquired standard photolithographic masks which do not suffer from stitching and periodic errors. The use of the new masks eliminated the periodic error in the dispersion direction in G1 and G3. We still observe low-level ghosts for G1 (see Fig. 5) on either side of the central peak, but these ghosts are displaced from the dispersion direction by an angle of ~30° and they appear to match the wavevector of the periodic wave front error noticeable in the optical interferometer surface error plot (left panel of Figure 4). A similar, but even smaller set of ghosts is observable in the 2-dimensional PSF plot for

G3 (not shown). We decided to apply the analysis appropriate for Rowland ghosts and compare the results to the interferometer data in order to determine whether the periodic pattern really is the source of ghosts in these two gratings. The relationship between the period of the spacing error and the distance of the Rowland ghost from the parent line in Littrow configuration is given by[15]:

$$\Delta x_M = M \frac{\lambda f}{P \cos \delta}$$

where Δx_M is the distance between the parent line and M-th order Rowland ghost, M is the ghost order, and P is the period of the spacing error. From Eq. 5, we deduce P = 5.6 mm for G1 and P = 0.61 mm for G3. In the wave front space observed in the interferogram, these distances will be shortened by $\cos\delta$ in the cross-dispersion direction. The projected period in the wavefront space is 5.1 mm which agrees well with the measured 4.0 mm from the fringes seen in the left panel of Figure 4. The displacement of the ghosts from the dispersion direction and the size of the period indicates that the spacing error is not due to errors in the mask pattern but rather to problems during the contact printing of the mask lines onto the photoresist layer which we also confirmed visually by observing interference fringes while contacting the mask with the photoresist coated disks.

The relationship between the ghost intensity and the parent line intensity for the first pair of Rowland ghosts is given by[15]:

$$\frac{I_{ghost}}{I_{line}} = \left(\frac{2\pi n}{\lambda} A \sin \delta \right)^2$$

where A is the amplitude of the spacing error, and I_{ghost} and I_{line} are intensities of the ghost pair and the parent line respectively. We derive A = 23 nm for G1 and A = 9.2 nm for G3. From the interferogram of G1, we estimate A = 28 nm/$\sin\delta$= 31 nm in excellent agreement with the direct measurement. The integrated intensity in the ghosts is 8.2% and 0.5% of the parent line intensities for G1 and G3 respectively at 1.523 μm in immersion.

Depending on the application, the ghosts seen in our gratings may not represent a problem. Since they are displaced in the spatial direction as well as dispersion direction, we can define the extent of each order in a cross dispersed spectrograph so that it excludes the contribution from ghost lines. Since the intensities scale as $1/\lambda^2$, the integrated intensity in both ghosts in G1 will drop to less than 2% at 3.1 μm.

4. SUMMARY

We have successfully completed a high quality immersion grating (G1) suitable for use in a high resolution near-infrared spectrometer. Several other, even better, immersion gratings have been completed except for their final antireflection coatings on the entrance faces and metallization of the grating grooves. We have tested the completed gratings, measuring their optical performance in several independent ways and used a variety of techniques to measure the properties of the grooves, groove surfaces, and coating layers. All of the results point to the conclusion that we can now reliably produce high performance, physically robust devices.

An intercomparison of different techniques shows that optical tests in a bench spectrometer, both testing devices at optical wavelengths as front-surface devices and in the near-IR in immersion, and optical interferograms of the diffracted wavefront give consistent results about the quality of our silicon diffraction gratings. This consistency adds to the reliability of the measured numbers. Our efficiency measurements at 1.523 μm for the completed grating G1 show that, on blaze, it will return ~70% of the incident light in the desired diffraction order. This efficiency is comparable to the performance of the best commercially available front-surface echelle gratings, even paying the penalty of transmission losses at the entrance/exit face of the immersion device. The theoretical diffraction limited resolving power of G1 is R = 200,000 at 1.5 μm. Spectrometer measurements in immersion with a modest IR beam

demonstrate R = 75,000 and the spectral PSF derived from optical interferometry over a larger area suggests that we can achieve even higher resolving powers with larger beamsizes.

The high refractive index of silicon will allow an instrument using the completed R2 immersion grating G1 to achieve R = 50,000 with a slit subtending 1.3/D arcseconds, where D is the telescope diameter in meters, with only a 23 mm collimated beam. The coarse groove spacing of this immersion grating makes possible designs covering a substantial contiguous fraction of an infrared atmospheric window in a single exposure.

Optically, the one fly in the ointment is the presence of low-level Rowland ghosts in G1. These ghosts are small and close enough to the main diffraction spike that they could potentially present a problem only at the shortest wavelengths and smallest slit widths. A careful investigation of our process leads us to believe that we understand the source of these ghosts. The complete but uncoated gratings in our last series show ghosts from repetitive errors at much lower levels and we are introducing several process improvements to eliminate even these small defects in our next series of devices.

Measurement of our groove surfaces using profilometry and atomic force microscopy shows that the groove surfaces are extremely flat and that the small-scale roughness is not a major contributor to the grating losses. The rms roughness measured with AFM indicates that <0.1% of the incident infrared radiation goes into diffuse scattered light.

The robustness of our completed devices is also good. We have performed thermal torture tests of the antireflection coatings and the aluminum reflective layers on silicon witness pieces to verify that they survive multiple rapid cyclings between room temperature and 77 K. Both the BBAR coatings and the Al layers survive well even under such harsh treatment.

We are currently working to improve the quality and increase the size of our immersion devices. The Rowland ghosts are the dominant contributor to the current error budget. Once these are reduced or eliminated, typical groove position errors could be as low as $\lambda/60$ at 632.8 nm for an R2 echelle grating. Instruments for 8 m and larger telescopes[16] will require immersion gratings 2-4 times larger than our completed devices. The scale-up does not present any substantial obstacles but will require a rethinking of several critical process steps, most notably the spin-on of the photoemulsion. We expect to be ready to produce larger devices within the next several years.

4.1. Acknowledgements

This work is supported by NASA grants NAG5-9230, NGTS5-137, and NNG06GC45, and also by funding from the Welch Foundation, and McDonald Observatory at the University of Texas at Austin. Fabrication and testing of the immersion gratings and silicon grism devices were made possible by facilities at the University of Texas at Austin, including the Center for Nano and Molecular Science and Technology (CNM) and the Microelectronics Research Center (MRC), funded in part by the National Science Foundation through the National Nanotechnology Infrastructure Network (NNIN). We thank R. Joyce, K. Hinkle, and G. Poczulp of NOAO for interferometer measurements. We thank K. Allers and S. Joshi for assistance in process development, and T. Gaubert and W. Frey for help with AFM measurements.

REFERENCES

1. K. H. Hinkle, R. W. Cuberly, N. A. Gaughan, J. B. Heynssens, J., R. R. Joyce, S. T. Ridgway, P. Schmitt, and J. E. Simmons, "Phoenix: A Cryogenic High-Resolution 1- to 5-um Infrared Spectrograph", *Proc. SPIE* **3354,** 810-821 (1998).
2. T. P. Greene, A. T. Tokunaga, D. W. Toomey, and J. S. Carr, "CSHELL: A high spectral resolution 1-5 µm cryogenic echelle spectrograph for the IRTF", *Proc. SPIE* **1946**, 313-324 (1993).
3. I. S. McLean, E. E. Becklin, O. Bendiksen, G. Brims, J. Canfield, D. F. Figer, J. R. Graham, J. Hare, F. Lacayanga, J. E. Larkin, S. B. Larson, N. Levenson, N. Magnone, H. Teplitz, and W. Wong. "Design and development of NIRSPEC: a near-infrared echelle spectrograph for the Keck II telescope", *Proc. SPIE*, **3354**, 566-578 (1998).

4. G. Wiedemann, B. Delabre, G. Huster, A. F. Moorwood, and B. Sokar, "High-resolution infrared echelle spectrograph (CRIRES) for the VLT", *Proc. SPIE* **4008**, 1076-1083 (2000).
5. H. Y. Fan and M. Becker, "Infra-Red Absorption of Silicon", *Phys. Rev.* **78**, 178-179 (1950).
6. W. R. Runyan, *Silicon Semiconductor Technology,* McGraw-Hill, New York (1965).
7. D. J. Mar, J. P. Marsh, and D. T. Jaffe, "Performance of large chemically etched silicon grisms for infrared spectroscopy", *Proc. SPIE*, this volume.
8. L. D. Keller, D. T. Jaffe, O. A. Ershov, T. Benedict, and U. U. Graf, "Fabrication and testing of chemically micromachined silicon echelle gratings", *Appl. Optics* **39**, 1094-1105 (2000).
9. O. A. Ershov, D. T. Jaffe, J. P. Marsh, and L. D. Keller, "Production of high-order micromachined silicon echelles on optically flat substrates", *Proc. SPIE* **4440**, 301-308 (2001).
10. O. A. Ershov, J. P. Marsh, K. N. Allers, and D. T. Jaffe, "Infrared grisms using anisotropic etching of silicon to produce a highly asymmetric groove profile", *Proc. SPIE* **4850**, 805-812 (2003).
11. J. P. Marsh, O. A. Ershov, and D. T. Jaffe, "Silicon grisms and immersion gratings produced by anisotropic etching: testing and analysis", *Proc. SPIE* **4850**, 797-804 (2003).
12. J. P. Marsh, "Production and Evaluation of Silicon Diffractive Optics for Infrared Astronomy", Ph.D. dissertation, The University of Texas at Austin, (2006).
13. E. W. Palmer, M. C. Hutley, A. Franks, J. F. Verrill, and B. Gale, "Diffraction gratings", *Rep. Prog. Phys*. **38**, 975-1048 (1975).
14. J. M. Bennett and L. Mattsson, *Introduction to Surface Roughness and Scattering*. Washington, Optical Society of America, (1999).
15. G. W. Stroke, "Diffraction gratings", *Handbuch der Physik* **29**, 426-758 (1967).
16. D. T. Jaffe, D. J. Mar, D. Warren, and P. R. Segura, "GMTNIRS – the High-Resolution Near-IR Spectrograph for the Giant Magellan Telescope", *Proc. SPIE*, this volume.